Supplementary Materials

Mutual information matrices

The raw pairwise mutual information is a matrix, where each element *i*, *j* corresponds to the mutual information between residues *i* and *j*. Because there is very low MI between most pairs of residues, it is informative to visualize this information as a sparse graph, as shown in the main text. However, a matrix can provide a complete representation of all the pairwise interactions in a way that a graph embedding cannot. Those data are shown here:

Figure S1: Raw mutual information matrices for TEM-1 (left) and CTX-M-9 (right) are sparse.

We might further be interested in the dependence of the mutual information on finite sampling. We thus performed 100 rounds of bootstrapping wherein N simulation trajectories were drawn at random with replacement from our set of simulations. To estimate error, we computed the standard deviation of the values of the mutual information that is computed on the bootstrapped data.

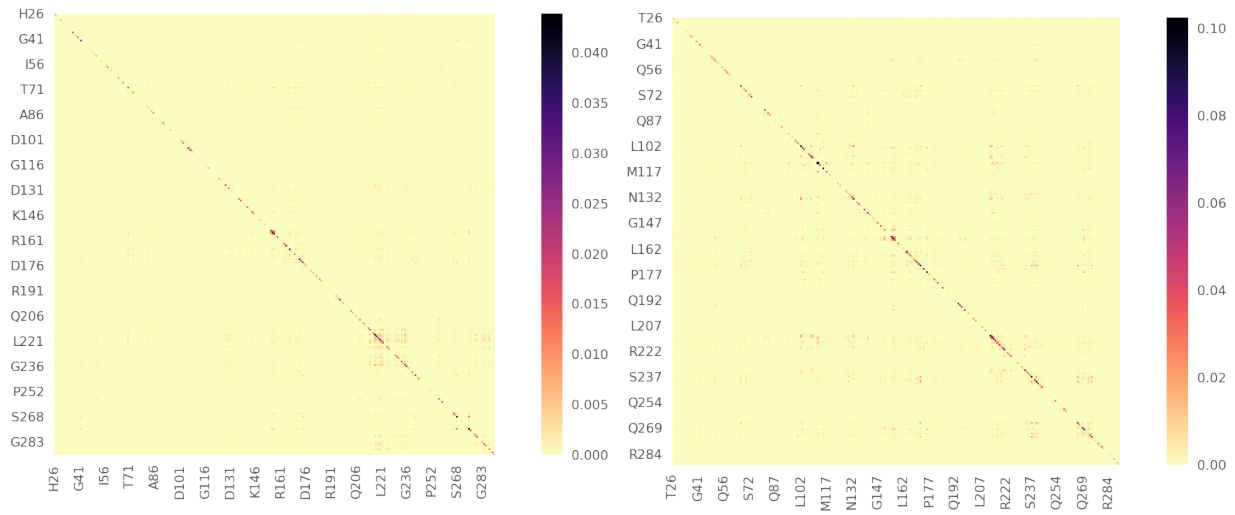

Figure S2: Bootstrapped error of mutual information matrices for TEM-1 (left) and CTX-M-9 (right) is globally low compared to raw mutual information (Fig S1).

We further were interested in how the variability would affect the absolute value of the mutual information. For this reason, we plotted rows of the mutual information with error bars for a few residues of interest.

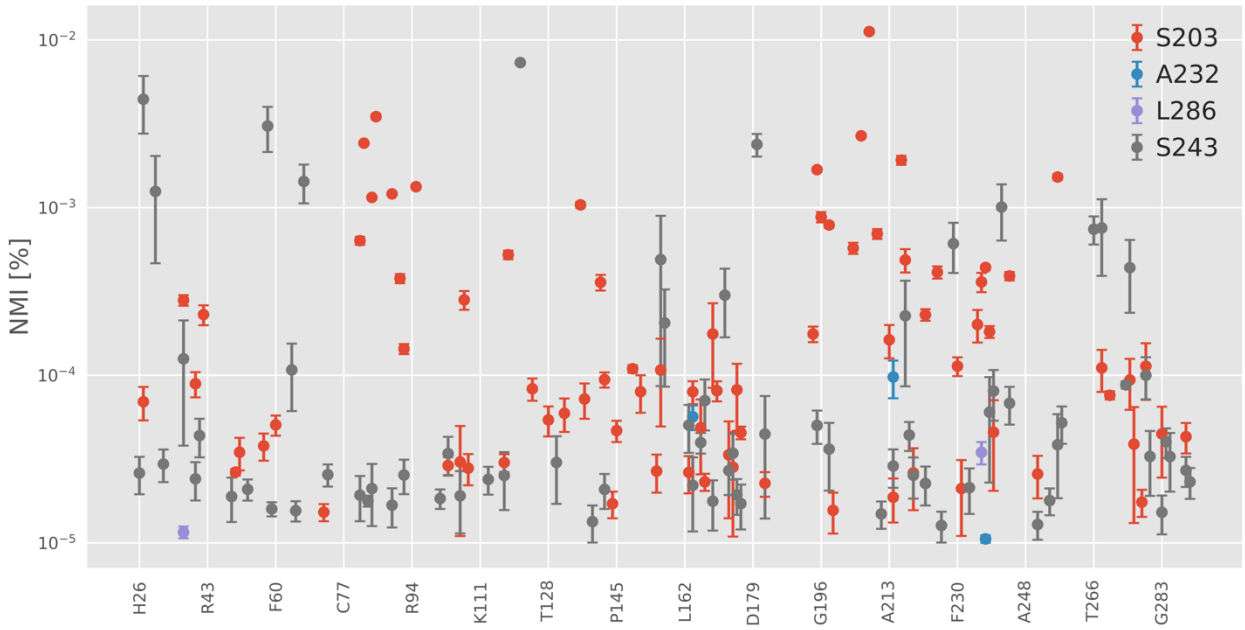

Figure S3: Residue pairs with high normalized mutual information have low bootstrapped error compared to their values. Each point represents the mutual information between the residue indicated by the color of the point and the residue indicated on the x-axis. All the points of a single color thus represent an entire row of the normalized MI matrix. Error bars are the standard deviation of 100 trials of bootstrapping.

SASA-eigenvector correlations confirm that most exposons are slow

To identify the principal motions giving rise to the exposure or burial of various residues, we compute Pearson's correlation coefficient between the eigenvectors' weights and the solvent accessibility of each residue. This yields an $n_{\mathrm{res}} \times n_{\mathrm{eig}}$ matrix. We capped the number of eigenvectors at 500 because any additional eigenvectors tend to correspond to very fast, less relevant motions.

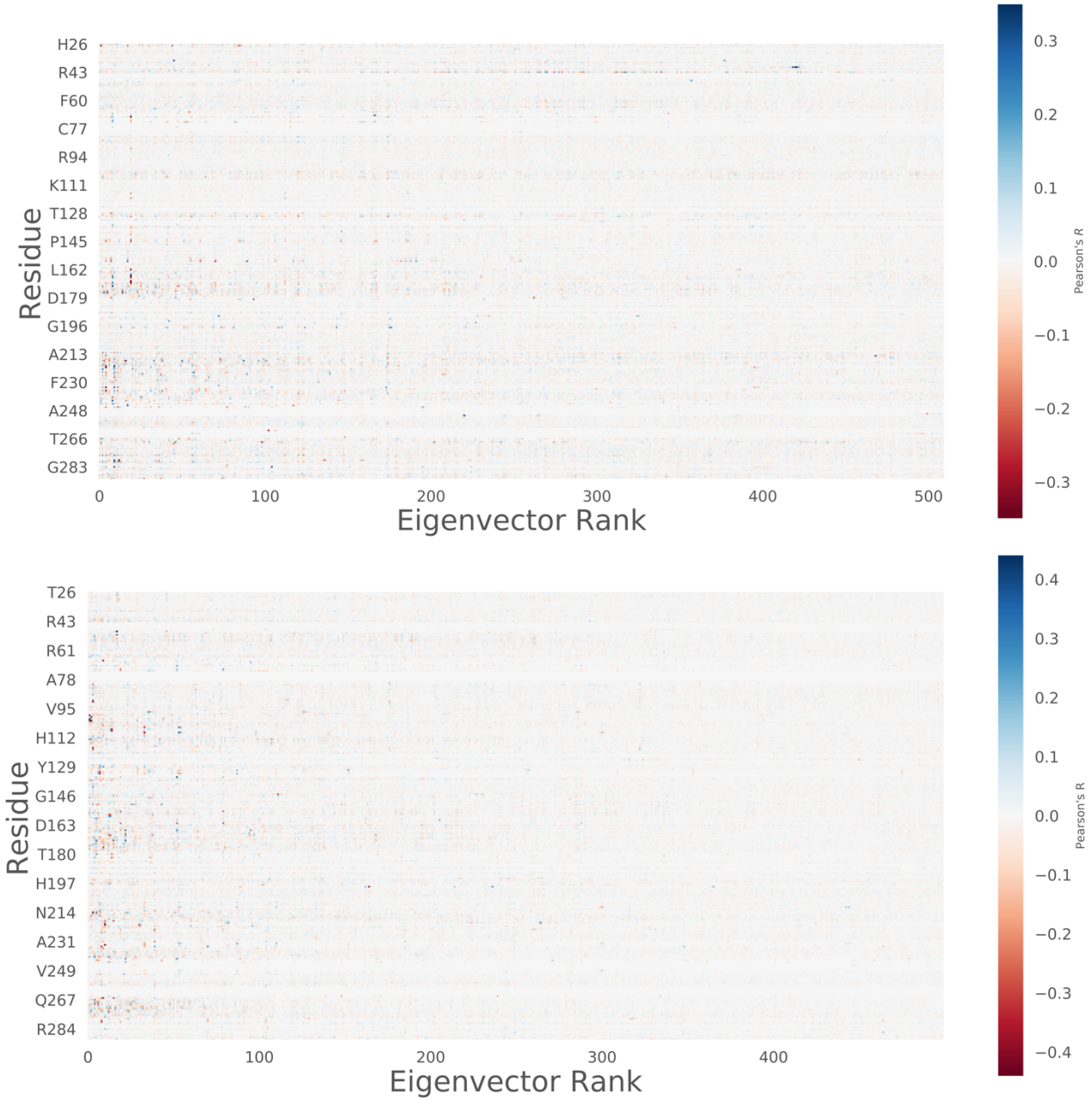

Figure S4: Slower motions (lower eigenvector rank) tend to correlate better with solvent accessibility changes. Pearson's coefficient of correlation R between sidechain solvent

accessibility and eigenvector weight across all states for each residue and eigenvector for TEM-1 (top) and CTX-M-9 (bottom).

The maximum flux pathway between open and closed states contains structures very close to the ligand-bound state

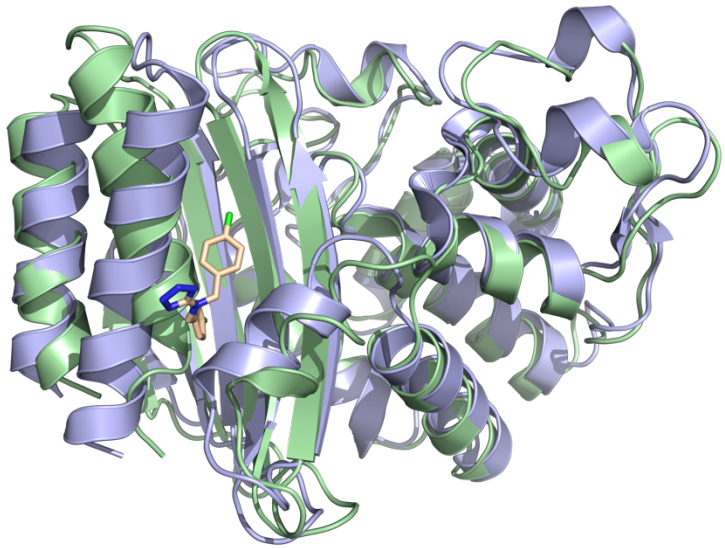

Figure S5: A structure from the maximum flux pathway between the extrema of the L286 eigenmode of TEM-1 (green) resembling even more closely the bound crystal structure of TEM-1 (blue) with CBT (yellow). Specifically, the extent of opening between the two helices forming the known TEM-1 allosteric pocket is similar in these two structures.

Estimation of druggability of S243 pocket

We used fpocket[1] to estimate the druggability of every frame associated with a microstate where S243 is classified as exposed. We then filtered pockets for S243 gamma oxygen involvement and for the lack of involvement of the active site serine, S70. As noted in the main text, traditional pocket detection algorithms have a tendency to combine this pocket with the active site, as they often form a channel-like connection, despite being geometrically distinct. We expect the druggabilities noted here to be lower bound estimates for druggability, the druggability score was trained on crystal structures of ligands, which are typically adopt a more closed conformation created by contributions of induced fit, whereas in simulation these same pockets are often much more open.[2]

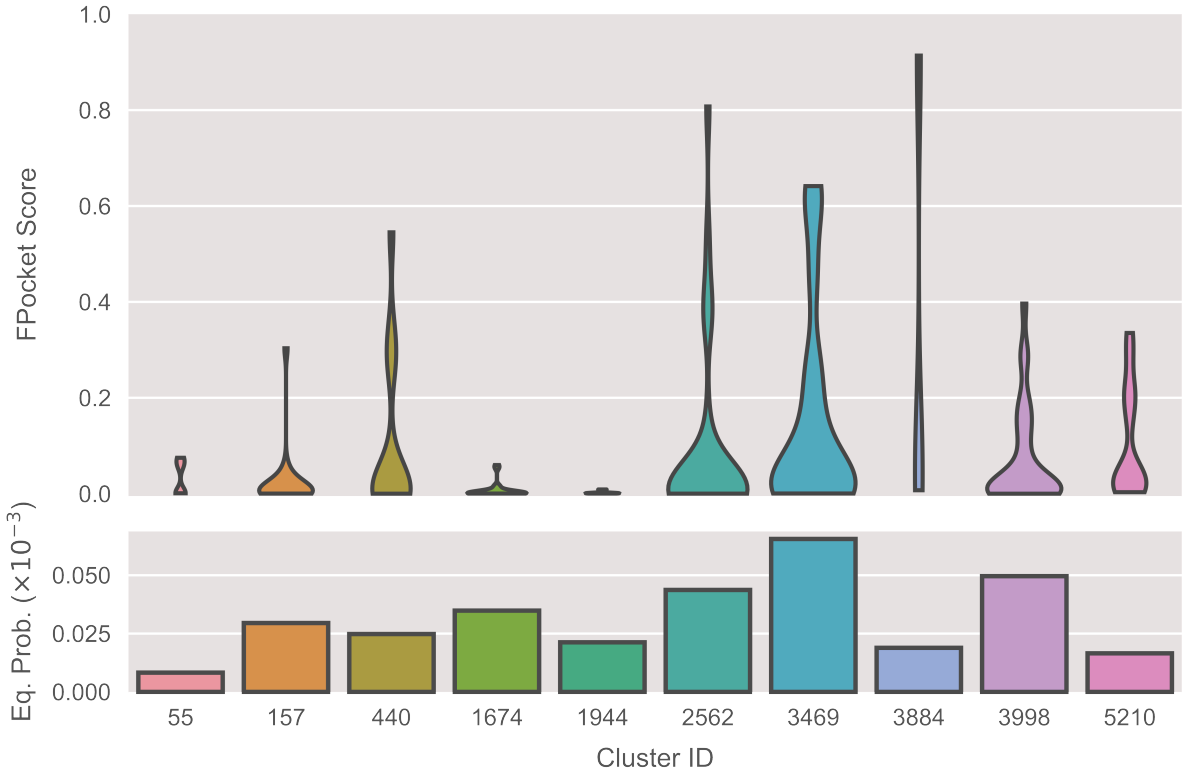

Figure S6: Druggability and equilibrium probabilities for pockets involving S243. *Top*, the distribution of FPocket druggability score for each microstate with exposed S243. *Bottom*, the equilibrium probability of each of those states. Two of the three most probable clusters (2562 and 3469) achieve scores above 0.5 (the proposed limit for druggability) and one (2562) produces pockets with scores exceeding 0.8.

Activity of labeled enzyme

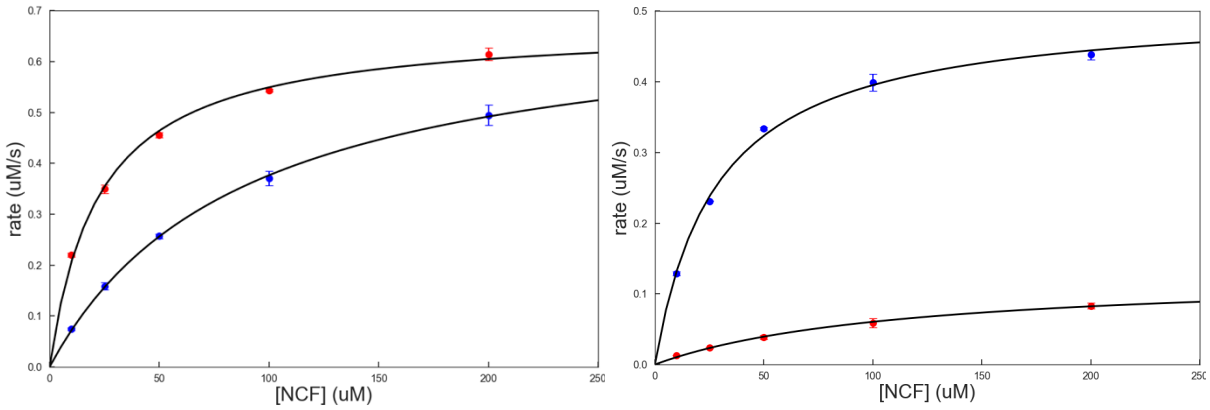

Figure S7: Activity of enzyme before (blue) and after (red) addition of covalent DTNB label for TEM-1 S243C (left) and CTX-M-9 (right). Blue points are unlabeled enzyme, red points are labeled enzyme. Points were taken in triplicate. Fits are to a Michaelis-Menten model.

Supplementary Table 1. Parameters for Michaelis-Menten model of enzyme activity. Error is the standard deviation from 100 trials of bootstrapping.

	k_{cat} (s^{-1})	K_M (μM)
TEM-1 M182T S243C	354 ± 13	88 ± 5
Labeled TEM-1 M182T S243C	337 ± 9	22 ± 2
CTX-M-9	254 ± 10	28 ± 3
Labeled CTX-M-9	65 ± 8	114 ± 21

Affinity clustering is stable to damping parameter changes

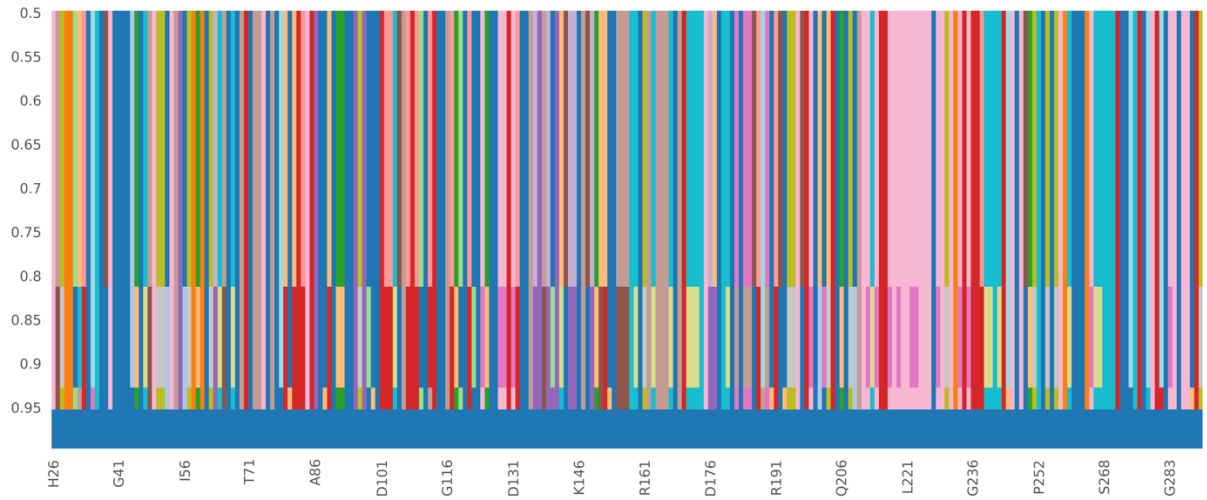

Figure S8: Affinity clustering is stable across most values of the damping parameter. In this figure, each row represents the assignment of each residue to a cluster for a particular choice of damping parameter. Each color denotes a single cluster. Thus, each vertical bar of color represents a range of damping parameter choices for which a residue is assigned to the same cluster. Hence, because there are few color perturbations in each column, many residues are assigned to the same cluster for all damping parameter choices < 0.95.

Markov State Model construction

We built our Markov state models using the discretization discovered by the khybrid clustering algorithm on SASA feature vectors (see Methods). We then verified our choice of kcenters stopping condition (2.6 nm^2 for TEM-1 and 3.0 nm^2 for CTX-M-9) and chose our lag times (4 ns for TEM-1 and 0.6 ns for CTX-M-9) using the implied timescales test.

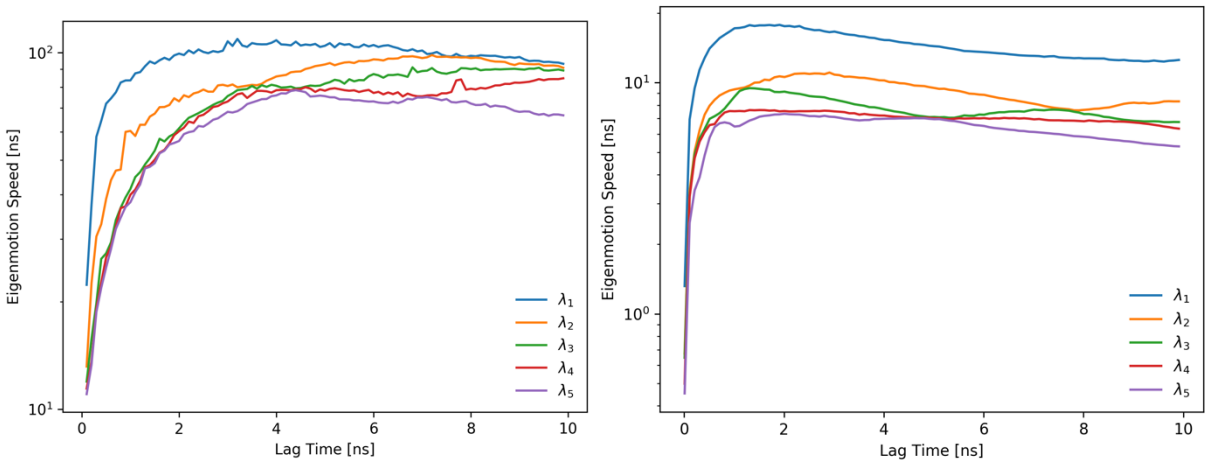

Figure S9: Implied timescales tests for TEM-1 (left) and CTX-M-9 (right).

Time-resolved DTNB thiol labeling by stopped-flow

To measure the labeling rate of any particular residue, we prepared the cysteine mutant (see *Methods*) and ran triplicate DNTB labeling experiments both with and without protein. We subtracted the baseline absorbance of DTNB in buffer from the labeling trace and fit to a single exponential. Each point in Fig 2b and e represents the results of such a procedure. A representative fit to the data for TEM-1 at 500 μM DTNB is shown below.

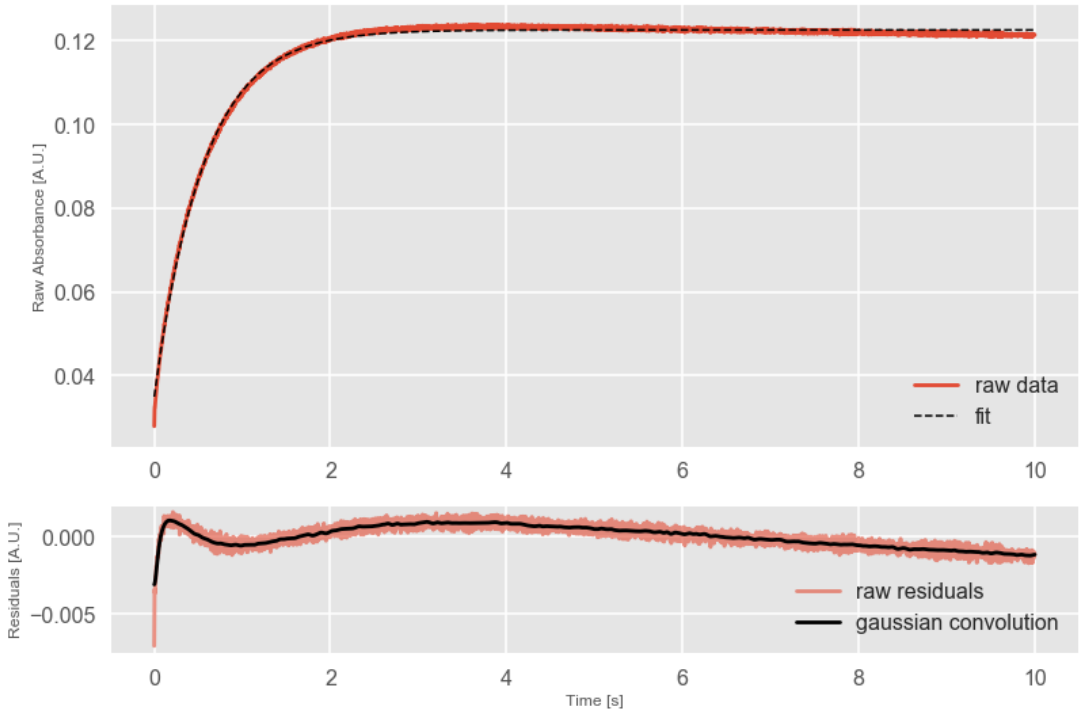

Fig S10: A representative trace of absorbance over time for a sample of 9 μM TEM-1 S243C mixed with 500 μM DTNB along with a single exponential fit (top) and the residuals to that same model (bottom). For the top figure, red is raw data and dashed black is the fit. For the bottom figure, red represents the raw residuals and black represents a Gaussian convolution of that data.

Supplementary Table 2. Parameters of Linderstrøm-Lang model of DTNB labeling. Error is the standard deviation from 100 trials of bootstrapping.

	TEM-1 M182T S243C	*CTX-M-9*
k_{int}	6.83 ± 1.18 mM^{-1} s^{-1}	71.5 ± 5.3 mM^{-1} s^{-1}
K	1.10 x 10^{-2} ± 1.9 x 10^{-3}	2.34 x 10^{-4} ± 7.8 x 10^{-5}
k_{op}	N/A	1.22 x 10^{-2} ± 2.05 x 10^{-3} s^{-1}
k_{cl}	N/A	51.3 ± 14.4 s^{-1}
$K \times k_{\text{int}}$	7.5 x 10^{-2} ± 1.5 x 10^{-3} mM^{-1} s^{-1}	1.67 x 10^{-2} ± 5.70 x 10^{-3} mM^{-1} s^{-1}

Measurement of TEM-1 S243C k_{int}

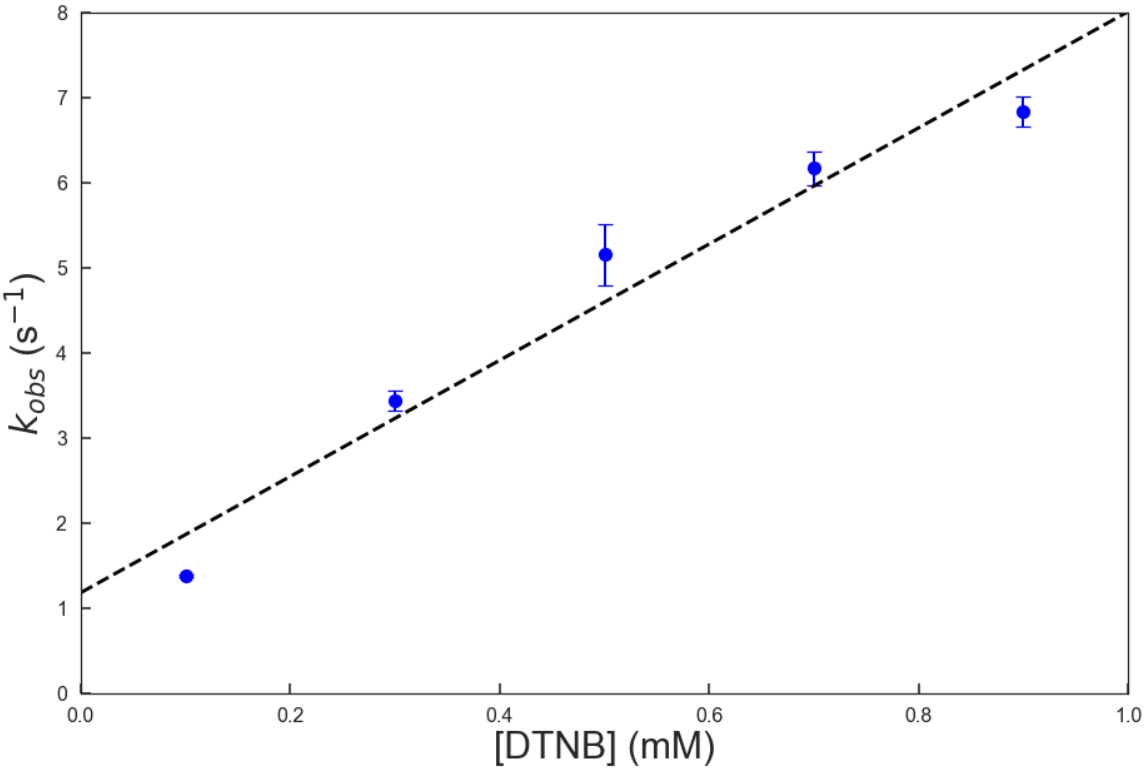

Figure S11: Rate of labeling TEM-1 S243C as a function of varying DTNB concentration in 6 M urea. The slope of the linear fit is the intrinsic rate of labeling (k_{int}) of this residue. Error is the standard deviation between triplicate runs at each DTNB concentration.

Estimation of global unfolding rates of TEM-1 S243C and CTX-M-9

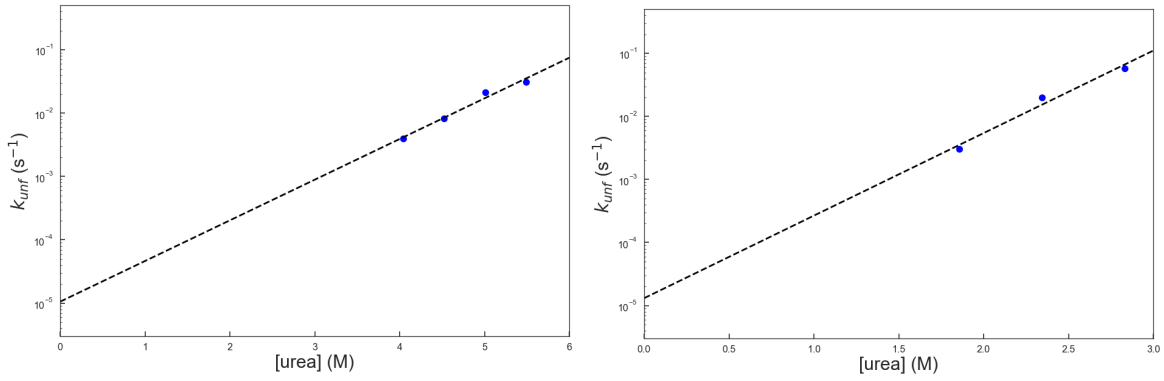

Fig S12: Rates of unfolding of TEM-1 S243C (top) and CTX-M-9 (bottom) as a function of urea concentration. A linear fit is used to extrapolate to the rate of global unfolding of each protein to the rate in the absence of urea. The rate of unfolding for TEM-1 S234C is 1.054 x $10^{-5} \pm 1.371$ x 10^{-5} s^{-1} whereas the rate of unfolding for CTXM9 is 1.308 x $10^{-5} \pm 2.274$ x 10^{-5} s^{-1}. Error is estimated using the standard deviation from 100 rounds of bootstrapping.

Protein stability measurements

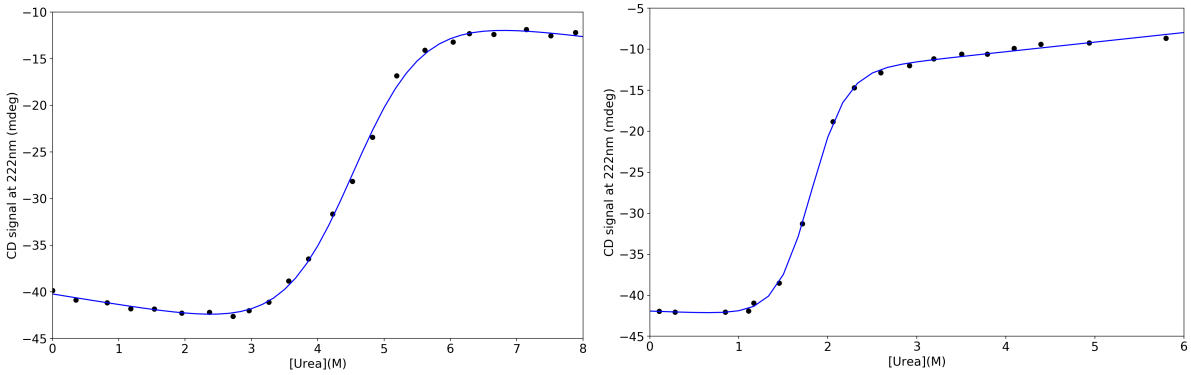

Fig S13: Circular dichroism as a function of urea concentration (solid circles) fit to a two-state model (equation S1) of unfolding for TEM-1 S243C (left) and CTX-M-9 (right).

$$(1)\ \mathrm{CD}\ (\Theta) = \frac{\Theta_u + \Theta_n e^{-(\Delta G_{un} + m_{un}[\mathrm{urea}])/RT}}{1 + e^{-(\Delta G_{un} + m_{un}[\mathrm{urea}])/RT}}$$

where Θ_u and Θ_n are the Circular Dichroism signals at 222 nm for the unfolded and native states. ΔG_{un} is the extrapolated free energy change in 0 M urea between the unfolded and native states, and m_{un} is a proportionality term related to the steepness of the linear fit of the unfolded to native state transition.[3]

Supplementary Table 3. Equilibrium Fit Parameters. Errors are standard deviations.

	ΔG_{un} (kcal mol^{-1})	m_{un} (kcal mol^{-1} M^{-1})	C_m (M)
TEM-1 M182T S243C	5.0 ± 0.3	1.12 ± 0.07	4.5 ± 0.4
CTX-M-9	5.5 ± 0.2	3.0 ± 0.1	1.83 ± 0.09

Observed labeling is bounded above by EX1 and EX2 labeling rates.

As defined in *Methods* of the main text, the observed labeling rates of the three regimes are defined as:

$$k_{\text{obs}} = \frac{k_{\text{op}} k_{\text{int}}[\text{DTNB}]}{k_{\text{op}} + k_{\text{cl}} + k_{\text{int}}[\text{DTNB}]}$$

$$k_{\text{obs}}^{(\text{EX2})} = \frac{k_{\text{op}}}{k_{\text{cl}}} k_{\text{int}}[\text{DTNB}] = K k_{\text{int}}[\text{DTNB}]$$

$$k_{\text{obs}}^{(\text{EX1})} = k_{\text{op}}$$

We want to show that $k_{\text{obs}} < k_{\text{obs}}^{(\text{EX2})}$ and $k_{\text{obs}} < k_{\text{obs}}^{(\text{EX1})}$.

Hypothesis I: $\boldsymbol{k_{\text{obs}} < k_{\text{obs}}^{(\text{EX2})}}$

$$k_{\text{obs}} < k_{\text{obs}}^{(\text{EX2})}$$

$$\frac{k_{\text{op}} k_{\text{int}}[\text{DTNB}]}{k_{\text{op}} + k_{\text{cl}} + k_{\text{int}}[\text{DTNB}]} < \frac{k_{\text{op}}}{k_{\text{cl}}} k_{\text{int}}[\text{DTNB}]$$

$$\frac{1}{k_{\text{op}} + k_{\text{cl}} + k_{\text{int}}[\text{DTNB}]} < \frac{1}{k_{\text{cl}}}$$

$$k_{\text{op}} + k_{\text{cl}} + k_{\text{int}}[\text{DTNB}] > k_{\text{cl}}$$

$k_{\text{op}} + k_{\text{int}}[\text{DTNB}] > 0$, which of course is true, since each term is greater than zero individually.

Hypothesis II: $k_{\text{obs}} < \boldsymbol{k_{\text{obs}}^{(\text{EX1})}}$

$$k_{\text{obs}} < k_{\text{obs}}^{(\text{EX1})}$$

$$\frac{k_{\text{op}} k_{\text{int}}[\text{DTNB}]}{k_{\text{op}} + k_{\text{cl}} + k_{\text{int}}[\text{DTNB}]} < k_{\text{op}}$$

$$\frac{k_{\text{int}}[\text{DTNB}]}{k_{\text{op}} + k_{\text{cl}} + k_{\text{int}}[\text{DTNB}]} < 1$$

$$k_{\text{int}}[\text{DTNB}] < k_{\text{op}} + k_{\text{cl}} + k_{\text{int}}[\text{DTNB}]$$

$0 < k_{\text{op}} + k_{\text{cl}}$, which of course is true, since each term is greater than zero individually.

Thus, since $k_{\mathrm{obs}} < k_{\mathrm{obs}}^{(\mathrm{EX2})}$ and $k_{\mathrm{obs}} < k_{\mathrm{obs}}^{(\mathrm{EX1})}$ we can conclude that $k_{\mathrm{obs}} < \min\left\{k_{\mathrm{obs}}^{(\mathrm{EX2})}, k_{\mathrm{obs}}^{(\mathrm{EX1})}\right\}$, i.e. that the EX1 and EX2 observed rates serve as strict upper bounds to the EXX observed rate.

References

1. Schmidtke, P. & Barril, X. Understanding and predicting druggability. A high-throughput method for detection of drug binding sites. *J. Med. Chem.* **53,** 5858–5867 (2010).
2. Bowman, G. R. & Geissler, P. L. Equilibrium fluctuations of a single folded protein reveal a multitude of potential cryptic allosteric sites. *Proc. Natl. Acad. Sci. U.S.A.* **109,** 11681–11686 (2012).
3. Bolen, D. W. & Santoro, M. M. Unfolding free energy changes determined by the linear extrapolation method. 2. Incorporation of delta G degrees N-U values in a thermodynamic cycle. *Biochemistry* **27,** 8069–8074 (1988).